This article appears in IFAC Mechatronics
https://doi.org/10.1016/j.mechatronics.2017.10.008

Deflection Modeling for a Needle Actuated by Lateral Force and Axial Rotation During Insertion in Soft Phantom Tissue

Thomas Lehmann[a,1,*], Carlos Rossa[a], Nawaid Usmani[b], Ronald Sloboda[b], Mahdi Tavakoli[a]

[a]*Department of Electrical and Computer Engineering, University of Alberta, Edmonton, AB, Canada, T6G 1H9*
[b]*Cross Cancer Institute and Department of Oncology, University of Alberta, Edmonton, AB, Canada T6G 1Z2*

Abstract

In prostate brachytherapy, radioactive seeds are implanted into the prostate for treatment of early-stage localized cancer. A major issue is seed displacement due to needle deflection, which is difficult to control as the needle is inserted manually. To address the problem and automate needle insertion, robotic systems, mathematical models for estimation and prediction and control algorithms have been developed. The method of choice for robotic steering of beveled-tip needles is predominantly intermittent axial needle rotation since this re-aligns the beveled tip and thus re-directs the needle. In this work, we present a method for needle steering to supplement axial needle rotation. A point force applied laterally to the needle near its point of insertion into tissue is used to displace the needle perpendicularly relative to its insertion axis. An advantage of this method is that the lateral force provides a continuous control input and thus continuous deflection control as opposed to axial needle rotation by 180 degrees in the 2D case of planar needle steering. Further, more control over deflection is possible as the lateral force provides direct shape change for the needle and improves the under-actuated nature of the needle. In order to predict and estimate needle deflection during insertion while applying both lateral force and axial rotation, a mechanics- and energy-based model for needle deflection is developed. Both single-layer and multi-layer tissue can be modeled if the tissue layer thickness is known. The accuracy of the model is validated experimentally. A comparison between the measured tip deflection and the model-based estimate shows only a small error. Moreover, control and sensitivity studies are carried out through insertion simulations using the model. The studies show the potentials and limitations for needle deflection reduction with various combinations of lateral force application and intermittent 180 degrees axial needle rotation.

Keywords: Medical robotics; needle insertion; brachytherapy; needle actuation; modeling; deflection estimation

1. Introduction

Needle insertion is a minimally invasive procedure commonly used in biopsy, drug delivery, therapy, and ablation. One of the therapeutic procedures in which needles are inserted for the purpose of radiation therapy is prostate brachytherapy (from Greek "short distance" therapy). A schematic depicting the procedure is shown in Figure 1. In order to implant the seeds into the prostate, the needle is loaded with rice-grain-sized seeds and inserted into the prostate. When the final insertion depth is reached, the seeds are deposited by being pushed out of the needle as it is retracted. Multiple needle insertions are carried out at different locations on a 5 millimetre grid template (see Figure 1) such that seeds are distributed across the prostate volume affected with cancerous tissue. For the radiation emitted by the seeds to be distributed efficiently throughout the prostate, it is important for the seeds to be deposited at their pre-planned locations. The target locations are registered with the template holes and, therefore, it is essential for the needle to remain on a straight path during insertion. Due to the cutting-related asymmetric forces acting at the beveled tip of the needle during insertion, however, the needle naturally deflects from a straight trajectory, thus causing the seeds to be deposited away from their pre-planned location. The tip of brachytherapy needles is beveled for facilitation of seed deposition and tissue cutting. Moreover, the beveled needle tip provides some control over needle deflection as the direction of the bevel can be changed through axial needle rotation. Thus, in order to steer the needle back to a straight trajectory, the brachytherapist may rotate the needle about its axis of insertion by 180°. Rotation is done intermittently throughout insertion to avoid tissue damage and out-of-plane deflection. Intermittant 180° axial needle rotation reverts the bevel's direction and, therefore, the asymmetric force's direction and steers the needle in the opposite direction.

The above-mentioned method for needle steering and trajectory control can be automated using robotic assistance in order

[☆]This work was supported by the Canada Foundation for Innovation (CFI) under grant LOF 28241, the Alberta Innovation and Advanced Education Ministry under Small Equipment Grant RCP-12-021, the Natural Sciences and Engineering Research Council (NSERC) of Canada under grant CHRP 446520, the Canadian Institutes of Health Research (CIHR) under grant CPG 127768, the Alberta Innovates - Health Solutions (AIHS) under grant CRIO 201201232 and by a University of Alberta startup grant.

[*]Corresponding author
Email addresses: lehmann@ualberta.ca (Thomas Lehmann), carlos.rossa@uoit.ca (Carlos Rossa), nawaid.usmani@albertahealthservices.ca (Nawaid Usmani), ron.sloboda@albertahealthservices.ca (Ronald Sloboda), mahdi.tavakoli@ualberta.ca (Mahdi Tavakoli)
[1]*Address:* 11-203 Donadeo Innovation Centre for Engineering, 9211-116 Street NW, Edmonton, AB, Canada, T6G 1H9

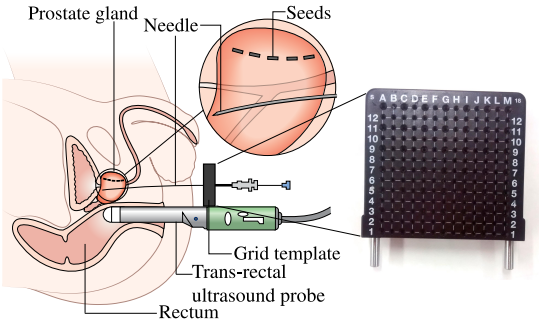

Figure 1: The radiation therapy procedure prostate brachytherapy. Radioactive seeds are inserted into the prostate with a needle guided by a grid template. The needle tip position is observed with a trans-rectal ultrasound (TRUS) probe (source: Cancer Research UK / Wikimedia Commons).

to aid the surgeon during needle insertion procedures. For improving the efficiency of seed deposition in brachytherapy or, more generally, steering of the needle tip towards a desired target, extensive research has been conducted in modeling needle-tissue interactions, sensing, estimation and prediction of needle deflection, and control algorithms for needle steering using axial rotation as the control action. Fundamental interactions between needle and tissue such as friction, and cutting-related tip forces were investigated [1, 2, 3, 4, 5]. Several contributions were made in further investigating needle-tissue interactions and proposing mechanics-based models for needle deflection [6, 7, 8, 5, 9, 10, 11, 12, 13, 14, 15, 16, 17]. Others proposed kinematics-based models [18, 19, 20, 21, 22], e.g., based on bicycle kinematics, which are less directly associated with tissue properties. The proposed models were then used to estimate or predict needle deflection [6, 23, 18, 7, 8, 9, 13, 15, 24, 17] in order to inform model-based controllers for needle steering using axial needle rotation [8, 9, 18, 19, 20, 21, 3, 25, 26, 24].

Further research was conducted on designs of robotic needle insertion systems for various clinical applications [27, 28, 29, 30, 31, 32]. Specifically for prostate brachytherapy, systems were developed that provide actuated guides that either complement or replace the fixed grid template (see Figure 1) for needle guidance and deflection manipulation during insertion [33, 34, 35, 36, 37]. For a recent and comprehensive literature review on issues in closed-loop needle steering see [38].

While axial needle rotation as a method for steering beveled tip needles has been investigated thoroughly in the past, a further method used by some brachytherapists in a manual fashion has received little consideration. Brachytherapist employing the method apply a force onto the needle perpendicular to the direction of needle insertion for the purpose of needle steering. The perpendicular force can be applied in close proximity to the needle insertion point and will henceforth be referred to as lateral force. It is applied with a finger near the needle's entry point into tissue counter to the direction of deflection in order to correct the needle tip deflection. The force is applied relatively early during insertion in order to force the entire needle shaft inside tissue to be displaced laterally. Towards the goal of utilizing this needle steering method during robot-assisted needle insertion, this paper provides a mechanics-based model that accounts for both steering actions: lateral force and axial needle rotation. A schematic depiction of the proposed method of lateral needle actuation is provided in Figure 2a. When using lateral force for needle steering, significant benefits exist. As the needle can be regarded as a highly under-actuated manipulator, the application of lateral force near the entry point into tissue provides an additional control input affecting the needle deflection more directly. Naturally, the beveled tip of the needle is constrained to move on a circular trajectory during insertion. This constraint can be significantly relaxed through lateral force as the needle tip can now be directly moved laterally thus increasing the needle tip's dexterity. The lateral force is a continuous input to a deflection control algorithm meaning that also the deflection can be influenced in a more continuous manner as opposed to intermittent axial rotation. If the goal is to keep the needle tip on a straight line (as it is assumed in seed deposition planning during prostate brachytherapy), the axial rotation input needs to be invoked continually to keep the tip deflection under a threshold. This is physically understandable due to the effect of the beveled tip, since as long as the needle insertion velocity is non-zero, its trajectory will diverge from a straight line. Since excessive use of axial rotation results in tissue drilling effects [39], the availability of an additional control input (the lateral force) that can reduce the amount of necessary axial needle rotations is highly beneficial.

A question we seek to answer particularly in the context of prostate brachytherapy is, to what extent can lateral force be used to manipulate the needle curvature for minimizing needle deflection and what are the existing limitations? It is assumed that the effect of the lateral force with respect to steering is reduced with increasing insertion depth. Responsible for this is decreasing resistance to needle bending with increasing needle length and confinement of the needle within tissue during insertion. Therefore, also lateral needle tip displacement caused by the lateral force and thus steerability are reduced at greater depths of lateral force application. This has also been hypothesized by Cowan *et al.* [40]. Moreover, it is of interest to know how lateral displacement and intermittent axial needle rotations should be combined to influence needle deflection and to properly steer the needle.

Due to the needle-tissue system's nonlinearity and constraints (e.g., limited needle maneuverability due to underactuation and non-holonomic properties), a model-based predictive control approach is necessary, which takes informed decisions based on prediction of needle deflection and on-line path planning. A requirement of controlling needle deflection in a predictive manner is therefore the development of a model, with which the needle curvature can be estimated and predicted based on the lateral needle displacement and axial needle rotation inputs. In this work, we introduce a model for the estimation of needle deflection resulting from a combination of applied lateral force and axial needle rotation. The model is energy-based and quasi-static, and its output is the needle deflection shape that occurs at a given insertion depth d.

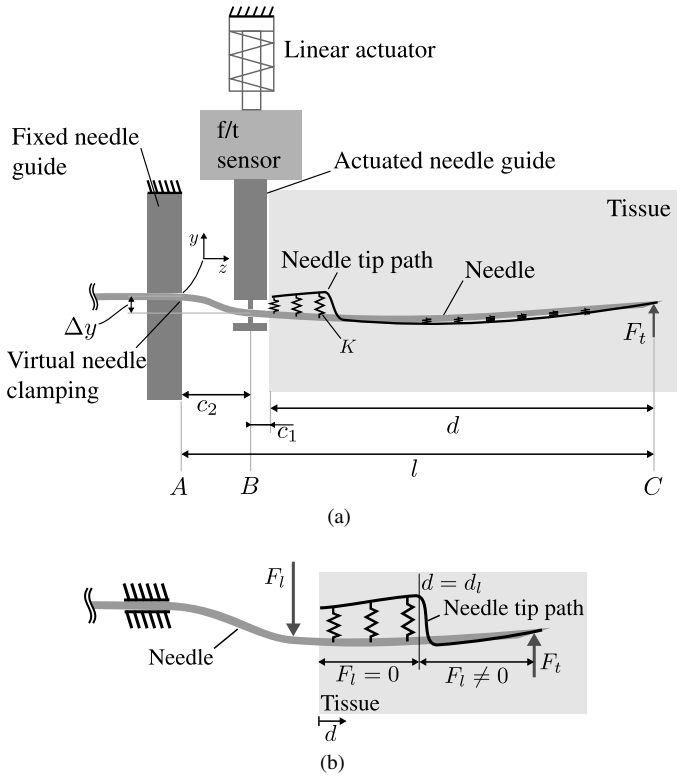

Figure 2: (a) A schematic of the needle being inserted into tissue with constraints enacted by the fixed needle guide and the actuated needle guide. The length l is the (variable) length of the needle section relevant for modeling and estimation. F_l is the force applied to the needle by the displacement of the actuated needle guide by Δy, which is measured by the f/t sensor. F_t is a tip-cutting-related point load. K is the tissue elasticity per unit distance modeled as elastic springs. (b) A close-up of the needle inside tissue with a force F_l applied laterally near the needle entry point illustrating F_l's effects on the needle curvature. The difference between the needle deflection shape and tip path is used as the elongation of the elastic springs.

1.1. Related Work

In order to construct the model, the principle of minimum potential energy is used. This approach has been commonly applied in the past to model needle-tissue interactions and needle deflection during insertion. Misra *et al.* presented an energy-based mechanical model that takes into account needle bending (strain energy), needle-tissue interaction (compression and elasticity) and tip cutting work (tip force and rupture) [5, 9]. Roesthuis *et al.* [11] extended the model proposed by Misra *et al.* by modeling the resistive force due to tissue compression by a distributed load acting along the inserted needle portion and incorporating needle steering through axial rotation into the model. Another model that used an energy-based approach was proposed by Lee and Kim [17]. Rossa *et al.* [16] in their version of an energy-based model considered also a cutting-related tip force and a load along the inserted needle portion modeled by a set of elastic springs. The springs model the tissue's resistance to compression. The spring stiffness is the tissue's Young's modulus. To determine the amount of tissue compression at a given position along the needle, the difference between the needle shaft shape and the needle tip trajectory, also referred to as the tip path, is considered. Moreover, the (stationary) grid template commonly used in prostate brachytherapy (see Figure 1) is included in the model.

1.2. Objectives & Contributions

This work proposes a novel method for automated needle trajectory manipulation during needle insertion into soft tissue based on two needle deflection manipulation methods commonly used during prostate brachytherapy, i.e., lateral force application and axial needle rotation. First, a model is presented, which describes the needle-tissue system during insertion with the two manipulation methods applied. The model is developed for the purpose of predicting and estimating needle deflection during insertion into single- and multi-layer tissue. It extends the approach proposed by Rossa *et al.* to incorporate the actuated needle guide depicted schematically in Figure 2a.

Our model is validated through insertion experiments carried out into phantom tissue samples under varying experimental conditions. The tuned conditions are lateral force magnitude F_l, depth of force application F_l and depth of 180° axial needle rotation. The experimental validations of the model are carried out with our custom-built prototype robotic assistant system. The robotic system is designed to assist surgeons during prostate brachytherapy and can be integrated into a clinical brachytherapy needle insertion setup without imposing much change on the surgical setup or the procedure. The system is designed to carry out steering actions that would otherwise be carried out manually by the surgeon.

Further, control simulation and parameter sensitivity studies are performed to assess the added benefits of the lateral force on needle deflection reduction and the limitations of the lateral force application for control. The results of these studies can inform model-based deflection controllers, which we intend to develop in the future as an extension to this work.

The paper is structured in the following order. In Section 2, the energy-based needle-tissue interaction model and solution for needle deflection are introduced. Section 3 provides an overview of the robotic assistant system prototype and the experimental setup for acquiring insertion data. Section 4 presents the results of the model validation experiments.

In Section 5 and Section 6, the results of the deflection control simulation and sensitivity study, respectively, are given. The results of Section 4, Section 5 and Section 6 are then discussed in Section 7. Finally, Section 8 offers concluding remarks and a brief outlook on our future work with regards to utilizing the work presented in this paper for model-based deflection control.

2. Needle-tissue Interaction Modeling & Deflection Estimation

This section introduces the modeling approach for needle-tissue interactions, followed by solving the model for needle deflection shape. The inputs to the model are the tip force F_t, with which needle rotation by 180° can be modeled, and the applied lateral force F_l. The model's output is needle deflection $u(z)$

with $z \in (0,l)$. The work presented in [16] is extended to incorporate a formulation for the actuated needle guide schematically depicted in Figure 2a. As the needle represents a slender beam that is clamped at one end and free at the other end, it is modeled as a cantilever beam. For the mathematical modeling of the needle-tissue system and the needle deflection occurring during insertion into tissue, Euler-Bernoulli beam theory is applied. A requirement for using Euler-Bernoulli beam theory for modeling of beam deflection is that the maximum deflection must be limited to approximately 10% of the overall beam length. With an overall needle length of up to 200 mm (e.g., a standard Brachytherapy needle) and a maximum deflection of approximately 10 mm (see Section 4.1), this requirement is satisfied. The model is quasi-static as in each insertion step, equilibrium conditions are assumed.

As shown in Figure 2a, counter to previous work, only the needle section from points A to C is considered for modeling since the needle bending to the left side of the fixed needle guide is not relevant. This also decreases the mathematical complexity of the model, which is an important advantage for computational efficiency. The fixed needle guide is modeled as a virtual clamping at point A and the needle is considered as a beam with increasing length in each step during insertion such that the needle length l is a variable. Two point loads are applied at points B and C, respectively, and a distributed load modeled as linear springs acts along the inserted needle portion. The actuated needle guide applies a lateral point force (F_l) onto the point B proximal to the needle's entry point into tissue. The needle is displaced laterally through the applied force F_l by the guide. The needle guide essentially acts as a fulcrum, which can be displaced perpendicularly relative to the needle's insertion axis and about which the needle can pivot such that its slope can change. By applying lateral force and thus displacement in the appropriate direction, the path that the needle follows inside tissue can be manipulated (see Figure 2b). The model is also designed to model multi-layer tissue where the amount of discrete layers are theoretically unlimited provided that the layer thickness is known.

2.1. Needle-Tissue System Model

The principle of minimum potential energy is used to formulate a mathematical model of the actuated needle-tissue system. The formulation captures the energy stored in the bent needle during insertion and the work applied to the needle-tissue system in the form of a functional, which is then transformed into a linear system of equations using the Rayleigh-Ritz method [41]. Finally, the linear system of equations is solved for the needle deflection shape.

The system potential, which is the energy stored in the bent needle and tissue during insertion and the work applied to the needle-tissue system, is

$$\begin{aligned} \Pi(u) &= U(u) + V \\ &= U_s(u) + U_d(u) + V_g + V_c \end{aligned} \tag{1}$$

where $U(u)$ is the energy stored in the system due to needle displacement and V is the work applied to the system by the actuated needle guide (force F_l) and the needle tip (force F_t). U_s is the strain energy due to the bending of the needle and U_d is the energy stored in the displaced tissue. V_g and V_c are the works done by the actuated needle guide (F_l) at point B and the tip force F_t at point C, respectively. In the following, each of the terms appearing in (1) are detailed.

2.1.1. Strain energy U_s

As the needle bends during insertion into tissue, strain energy is stored in the needle, which is expressed as

$$U_s(u) = \int_0^l \frac{EI}{2} \left(\frac{\partial^2 u(d,z)}{\partial z^2} \right)^2 dz \tag{2}$$

where z is the horizontal coordinate, E and I are the needle's Young's modulus and area moment of inertia, respectively, l is the needle length and $u(d,z)$ is the needle deflection shape at insertion depth d and z.

2.1.2. Potential Energy Stored in Displaced Tissue U_d

As the needle deflects as it is inserted into tissue, the tissue surrounding the needle is displaced. The energy stored in the compressed single-layer tissue can be expressed as:

$$U_d(u) = \frac{K}{2} \int_{l-d}^{l} \Big(u(d,z) - u_t(d,z) \Big)^2 dz \tag{3}$$

where $u_t(d,z)$ is the (recorded or estimated) path taken by the needle tip during insertion (needle tip path, see Figure 2), K is the tissue stiffness expressed as force per unit length and d is the insertion depth.The tissue reaction is represented as virtual springs acting along the inserted needle portion as shown in Figure 2. The springs connect the needle shaft to the needle tip path. Thus, the loading of the springs is dependent on the difference between the needle tip path u_t and the needle shaft deflection u at a point z along the needle as shown in (3) and Figure 2a.

When for example two-layer tissue is considered, the integral in (3) can be separated as follows:

$$\begin{aligned} U_d(u) &= \frac{K_1}{2} \int_{l-d}^{l-d_K} \Big(u(d,z) - u_t(d,z) \Big)^2 dz \\ &\quad + \frac{K_2}{2} \int_{l-d_K}^{l} \Big(u(d,z) - u_t(d,z) \Big)^2 dz \end{aligned} \tag{4}$$

where d_K is the depth at which the tissue layer and therefore the tissue stiffness changes. Extending the modeling of tissue to an arbitrary amount of discrete layers is now trivial provided the tissue layer thickness or depth of stiffness change is known.

2.1.3. Work Done by the Actuated Guide

The work done by the lateral force F_l applied by the actuated needle guide at point B at distance c_2 from the fixed needle guide is expressed as

$$V_g = F_l u(d, c_2) \tag{5}$$

where $u(d,c_2)$ is the needle deflection at point B.

2.1.4. Work Done by the Tissue Cutting Force (F_t)

The tip force shown as F_t in Figure 2a is the predominant reason for needle deflection during insertion into tissue and is caused by the asymmetric geometry of the beveled needle tip. Due to the asymmetry, the tissue is displaced by the needle tip as the needle cuts through tissue. As a result of this, the needle deflects in the same direction as the bevel. Thus, the direction of F_t and the direction of deflection is determined by the orientation of the bevel. Upon needle rotation, the sign change of F_t needs to be carried out gradually (e.g., within 3 seconds. see Figure 6) in order to avoid a sudden jump in the needle deflection estimate. The work done by F_t is expressed as

$$V_c = F_t u(d,l) \tag{6}$$

where $u(d,l)$ is the needle tip deflection. It should be noted that the needle tip path $u_t(d,l)$ is different from the needle tip deflection $u(d,l)$ in that the needle tip path is constructed from tip deflections at past insertion steps and therefore depends on the horizontal coordinate z.

Finally, equations (2) - (6) are inserted into (1) to obtain the system energy model in the form of a functional:

$$\begin{aligned}\Pi(u) &= \int_0^l \frac{EI}{2}\left(\frac{\partial^2 u(d,z)}{\partial z^2}\right)^2 dz \\ &+\frac{K_1}{2}\int_{l-d}^{l-d_K}\Big(u(d,z)-u_t(d,z)\Big)^2 dz \\ &+\frac{K_2}{2}\int_{l-d_K}^{l}\Big(u(d,z)-u_t(d,z)\Big)^2 dz \\ &-F_l u(d,c_2) - F_t u(d,l)\end{aligned} \tag{7}$$

where the two-layer tissue case is considered in (7) and is also used for the following derivation of the deflection model.

2.2. Solving for Needle Deflection

In order to solve the above introduced energy-based model of the needle-tissue system for the needle deflection shape, as in previous works, the the Rayleigh-Ritz method is used. It is a variational method frequently applied to solve energy minimization problems and states that a differential equation in the form of a functional can be approximated by a finite sum of weighted shape functions. The following finite series represents the weighted shape functions [41]:

$$u_n(d,z) = \sum_{i=1}^{n} q_i(z) g_i(d) \tag{8}$$

Here, $q_i(z)$ is the i^{th} shape function and $g_i(d)$ is the corresponding weighting coefficient. $q_i(z)$ is given by [42, 14]:

$$\begin{aligned}q_i(z) &= \frac{1}{\kappa_i}\Bigg(\sin(\beta_i\frac{z}{l}) - \sinh(\beta_i\frac{z}{l}) \\ &-\gamma_i\Big[\cos(\beta_i\frac{z}{l}) - \cosh(\beta_i\frac{z}{l})\Big]\Bigg).\end{aligned} \tag{9}$$

and represents the i^{th} vibration mode. κ_i and γ_i are computed as

$$\begin{aligned}\gamma_i &= \frac{\sin\beta_i + \sinh\beta_i}{\cos\beta_i + \cosh\beta_i} \\ \kappa_i &= \sin\beta_i - \sinh\beta_i - \gamma_i(\cos\beta_i - \cosh\beta_i).\end{aligned} \tag{10}$$

The values of the constants β_i for a cantilever beam (clamped-free) are $\beta_1 = 1.857$, $\beta_2 = 4.695$, $\beta_3 = 7.855$, $\beta_4 = 10.996$, and $\beta_i \simeq \pi(i-1/2)$ for $i > 4$ [42]. The next step is to insert (8) into (7):

$$\begin{aligned}\Pi(u_n) &= \frac{EI}{2}\int_0^l\left(\sum_{i=1}^{n} q_i''(z)g_i(d)\right)^2 dz \\ &+\frac{K_1}{2}\int_{l-d}^{l-d_K}\left(\sum_{i=1}^{n} q_i(z)g_i(d) - u_t(d,z)\right)^2 dz \\ &+\frac{K_2}{2}\int_{l-d_K}^{l}\left(\sum_{i=1}^{n} q_i(z)g_i(d) - u_t(d,z)\right)^2 dz \\ &-F_l\sum_{i=1}^{n} q_i(c_2)g_i(d) - F_t\sum_{i=1}^{n} q_i(l)g_i(d)\end{aligned} \tag{11}$$

where $q''(z)$ denotes the second derivative of $q(z)$ with respect to z. The condition for minimizing the potential $\Pi(u_n)$ is that $\frac{\partial\Pi}{\partial g_j} = 0$ for $j = 1,\ldots,n$. Using this condition, a linear system of equations can be established and solved for the unknown weighting coefficients g_i. In the following step, we take the partial derivative of $\Pi(u_n)$ with respect to $g_j(d)$ while considering that $q_i(l) = q_j(l) = 1$, $\forall i,j$, (see (9)) and that $q_j(c_2)$, $\forall j$, is a known quantity:

$$\begin{aligned}\frac{\partial\Pi(u_n)}{\partial g_j(d)} =& EI\int_0^l\left(\sum_{i=1}^{n} q_i''(z)g_i(d)\right)q_j''(z)\,dz \\ &+K_1\int_{l-d}^{l-d_K}\left(\sum_{i=1}^{n} q_i(z)g_i(d) - u_t(d,z)\right)q_j(z)\,dz \\ &+K_2\int_{l-d_K}^{l}\left(\sum_{i=1}^{n} q_i(z)g_i(d) - u_t(d,z)\right)q_j(z)\,dz \\ &-F_l q_j(c_2) - F_t = 0.\end{aligned} \tag{12}$$

In order to simplify (12), the sum over index $i = 1,\ldots,n$ and $g_i(d)$ are extracted to obtain

$$\sum_{i=1}^{n}\phi_{ji}g_i(d) - \omega_j - \gamma_j - F_t = 0 \tag{13}$$

with

$$\begin{aligned}\phi_{ji}(z) &= EI\int_0^l q_i''(z)q_j''(z)\,dz \\ &+K_1\int_{l-d}^{l-d_K} q_i(z)q_j(z)\,dz + K_2\int_{l-d_K}^{l} q_i(z)q_j(z)\,dz \\ \omega_j(z) &= K_1\int_{l-d}^{l-d_K} u_t(d,z)q_j(z)\,dz + K_2\int_{l-d_K}^{l} u_t(d,z)q_j(z)\,dz \\ \gamma_j &= F_l q_j(c_2).\end{aligned}$$

(13) can now be re-written into a matrix formulation:

$$\Phi(z)\mathbf{g}(d) = \Gamma + F_t\mathbf{1}_{n\times 1} + \Omega(z) \tag{14}$$

with

$$\Phi = \begin{bmatrix} \phi_{11} & \cdots & \phi_{1n} \\ \vdots & \ddots & \vdots \\ \phi_{n1} & \cdots & \phi_{nn} \end{bmatrix}; \Gamma = \begin{bmatrix} \gamma_1 \\ \vdots \\ \gamma_n \end{bmatrix}; \Omega = \begin{bmatrix} \omega_1 \\ \vdots \\ \omega_n \end{bmatrix}; \mathbf{g} = \begin{bmatrix} g_1 \\ \vdots \\ g_n \end{bmatrix}$$

and where $\mathbf{1}_{n\times 1}$ is a column vector of ones of size n. Finally, we can solve for the unknown vector $\mathbf{g}$

$$\mathbf{g} = \Phi^{-1}\left(\Gamma + F_t\mathbf{1}_{n\times 1} + \Omega\right) \tag{15}$$

and insert (15) into (8) in order to calculate the estimated needle shape $u_n(d,z)$.

2.3. Model Parametrization

The model takes as parameters the tissue stiffness K and the needle tip force F_t. Here, the methods for obtaining K and F_t are introduced.

2.3.1. Tissue Stiffness K

The tissue stiffness K is measured physically via compression tests. The fact that the parameter K in the model is not dependent on u suggests that K is constant for the considered deflection. Thus, to determine K, Hooke's law $\sigma = K\varepsilon$ is used where σ is the stress resulting from the applied strain ε during the compression test. More specifics regarding the experimental setup used for compression tests are given in Section 4.1.1.

2.3.2. Tip force F_t

The second parameter to be obtained is the tip force F_t. To estimate the parameter, the needle tip deflection measured during insertion is used, combined with a modified version of (14) and the measured K. The measured needle tip deflection u_t and a special case of (9), which occurs at $z = l$ where $q_i(l) = 1\ \forall\ i$, can be used to obtain

$$u(d,l) = \sum_{i=1}^{n} g_i(d) = u_t. \tag{16}$$

Using (16), we can now expand (14) to $n+1$ equations as follows [43]:

$$\underbrace{\begin{bmatrix} \Phi & -\mathbf{1}_{n\times 1} \\ \mathbf{1}_{1\times n} & 0 \end{bmatrix}}_{\Phi^*} \underbrace{\begin{bmatrix} \mathbf{g} \\ F_t \end{bmatrix}}_{\mathbf{g}^*} = \underbrace{\begin{bmatrix} \Gamma \\ 0 \end{bmatrix}}_{\Gamma^*} + \underbrace{\begin{bmatrix} \Omega \\ 0 \end{bmatrix}}_{\Omega^*} + \underbrace{\begin{bmatrix} \mathbf{0}_{n\times 1} \\ u_t \end{bmatrix}}_{\Lambda}. \tag{17}$$

Finally, (17) can be solved for $\mathbf{g}^*$ as

$$\mathbf{g}^* = \Phi^{*-1}\left(\Gamma^* + \Omega^* + \Lambda\right) \tag{18}$$

in order to obtain the tip force F_t.

3. Robotic System Prototype for Manual Needle Insertion

The setup for needle insertion is depicted in Figure 3. It re-creates the setup used during prostate brachytherapy procedures. The actions to manipulate the needle's trajectory, namely the application of lateral force and axial rotation, are carried out automatically during insertion. The setup consists of a Hand-held Needle Steering Assistant (HNSA)[43] holding a standard 18G brachytherapy needle, a fixed needle guide and a second needle guide actuated by linear actuators and sensorized through a force/torque sensor mounted at its base. Furthermore, an actuated ultrasound (US) probe is used for tracking the needle tip inside the phantom tissue sample held by a transparent container.

The HNSA [43] contains a small rotary motor, with which the mounted needle can be automatically rotated about its axis. Affixed to the side of the HNSA are two optical markers used to continuously track its position during insertion with an optical tracker (MicronTracker, ClaroNav, Toronto, ON, Canada). The assistant's position is used to determine the needle insertion depth. The optical tracker is calibrated to the location of the tissue container. All components of the setup, except for the HNSA are mounted onto a breadboard in order to ensure experimental repeatability.

The fixed needle guide is a standard variant as used in prostate brachytherapy. It has a thickness of 20 millimeters and the holes are made to fit the 18G brachytherapy needle. As the fixed needle guide is mounted to the breadboard, the needle is restricted from moving laterally and pivoting within the template.

The actuated needle guide consists of two linear actuators (L16 Miniature Linear Actuator, Actuonix Motion Devices Inc., Victoria, BC, Canada). The actuators are mounted perpendicular to each other, which restricts the actuated guide's motions to a plane parallel to the fixed needle guide. In this work, however, only force in the horizontal direction is applied onto the needle as the needle's deflection remains on a horizontal plane during insertion. The vertical linear actuator is used to accurately align the actuated needle guide with a hole in the fixed needle guide and remains static during insertion. The actuator assembly's structural rigidity is ensured through two linear guides mounted in parallel to each linear actuator and perpendicular to each other. The vertical guide rail is mounted onto the horizontal guide rail's carriage. The forces exerted by the guide onto the needle are measured by a 6 degree-of-freedom (DOF) force/-torque (f/t) sensor (50M31A3-I25, JR3 Inc., Woodland, CA, USA). The f/t sensor is used to control the lateral force applied by the actuated guide through a PID force controller where the force signal obtained from the f/t sensor is filtered by a fourth order Butterworth filter. Due to the small hole depth (1.7 mm) of the actuated needle guide the needle can pivot within the guide and friction between guide and needle is negligible.

The US probe (4DL14-5/38 Linear 4D, Ultrasonix, Richmond, BC, Canada) is mounted onto a linear stage via a cross-bar structure, which is aligned parallel to the tissue container and actuated by a DC motor. Thus, the probe is restricted to move along the tissue in the direction of needle insertion. The

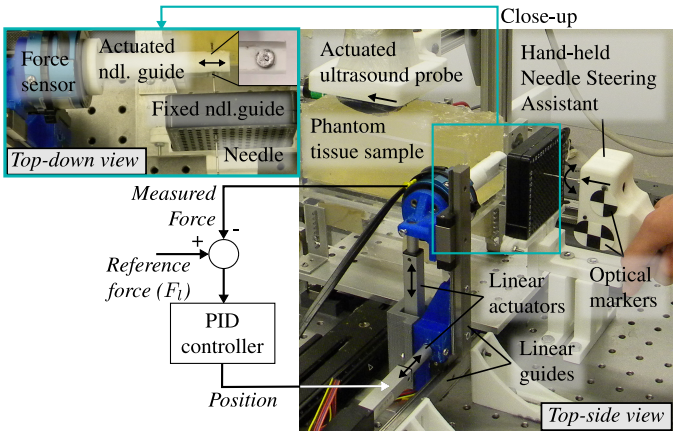

Figure 3: The experimental setup used for semi-manual needle insertions. During insertion, lateral force can be applied via linear actuators and the needle can be rotated axially through the Hand-held Needle Steering Assistant [43] at predefined insertion depths. The experimental setup re-creates the surgical setup for needle insertion during prostate brachytherapy.

position of the US probe is controlled such that it follows the needle tip during insertion using the relative position of the HNSA captured by the optical tracker as a reference. A diagnostic US system (SonixTOUCH, Ultrasonix, Richmond, BC, Canada) is used to generate US images from the sonography data acquired by the US probe. The US system records axial images of the needle inside tissue in order to track the needle tip position during insertion.

The images generated by the US system, in which the needle cross-section is marked as a bright spot, are processed with a needle tracking algorithm. The algorithm, which is a modified version of the one introduced by Carriere *et al.* [44], tracks the needle cross-section for the measurement of the needle tip deflection during insertion. The measured deflection is later used as ground truth for experimental validation of the proposed model. A source of noise in the deflection measurement is the fact that the shape and size of the bright spot marking the needle cross-section is subject to small fluctuations due to artifacts appearing in different sections of the tissue. These fluctuations translate into noise in the tracked needle deflection.

4. Model Validation

In this section, an experimental validation of the model proposed in Section 2 is given. The performance of the model for estimating the needle tip deflection during insertion into phantom tissue made from plastisol is presented. The needle tip deflection measured during insertion is compared to the tip deflection estimate through a statistical analysis.

4.1. Experimental Results

Six different experimental scenarios are chosen. The scenarios are listed in Table 1. The variables listed in Table 1 are described as follows. F_l is the magnitude of the lateral force applied onto the needle by the actuated guide near the needle's entry point into tissue, d_l represents the needle insertion depth in millimeters after which the lateral force F_l is applied by the actuated needle guide (see Figure 2b) and d_r is the 180° axial rotation depth in millimeters. In all scenarios where $F_l \neq 0$ N, the force F_l is removed at an insertion depth of 100 mm. The above choices were purposefully made with the intention to mimic steering actions performed by surgeons in a clinical scenario to reduce the deflection of the needle inside tissue. The sign of F_l is chosen such that its direction is against the direction of deflection caused by the needle tip bevel. By choosing scenarios with different depths d_l for application of the lateral force F_l, its effect on the magnitude of a deflection reduction will be shown. Since a combination of needle rotation and lateral force is modeled, the combined effect of F_l and rotation towards minimization of deflection is presented in scenario 3 (see Table 1). Thus, d_r is chosen such that the combined effect of F_l and rotation further reduce needle deflection. During scenario 5 and 6, the needle is inserted into a phantom tissue sample consisting of two tissue layers with different Young's moduli. These scenarios are considered to validate the multi-layer version of the deflection model where the model is provided with the two different layer stiffnesses and the thickness of the first layer. The interface depth of the two layers d_K is chosen to be 50 mm, a depth at which a human prostate is commonly located. Details regarding the quantification of the Young's moduli of the two layers are given in the following section.

Table 1: The four considered experimental scenarios.

Scenario #	Lateral force F_l [N]	Depth of application d_l [mm]	Rotation depth d_r [mm]	Tissue type
1	0	x	x	
2	-2.5	20	x	single
3	-2.5	20	100	layer
4	-2.5	45	x	
5	0	x	x	multi
6	-2.5	20	100	layer

For each scenario, six insertions are carried out. The needle used for the insertions is a standard hollow 18G (⌀ 1.27 mm) brachytherapy needle (Eckert & Ziegler BEBIG Inc., Oxford, CT, USA), which has a length of 200 mm and is made from stainless steel (Young's modulus $E = 200$ GPa). During scenario 1 to 4, the needle is inserted 24 times into the single-layer sample of phantom tissue made from Plastisol (5.0 Soft Plastisol, M-F Manufacturing, Fort Worth, TX, USA) and during scenarios 5 and 6, the needle is inserted 12 times into a two-layer plastisol tissue sample. The distance $c = c_1 + c_2$ (see Figure 2a) is set to 36 mm during scenario 1 to 4 and to 42 mm during scenario 5 and 6. In all scenarios, the distance c_1 is set to 9 mm.

4.1.1. Model Parameter Identification

Before a model estimate can be obtained, the parameters K and F_t need to be identified for the two tissue samples described above. Figure 4a shows the setup used for the compression

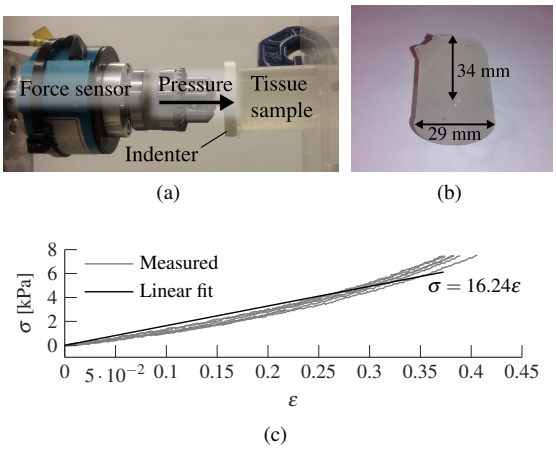

Figure 4: (a) The setup and (b) the tissue sample used for compression experiments. (c) Stress-strain curves for six trials of compression tests including a linear fit. The following stiffness was calculated for the homogeneous tissue sample: $K = \frac{\sigma}{\varepsilon} = 16.24$ kPa.

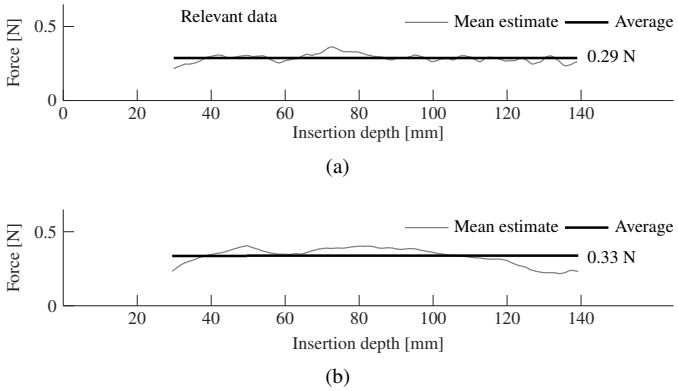

Figure 5: The needle tip force estimation results. The mean tip force estimate of six insertions according to (a) scenario 1 and (b) scenario 5 (see Table 1) obtained from (18) are plotted along with the averaged constant tip force F_t. The final estimate of the needle tip force is $F_t = 0.29$ N for the single-layer tissue sample and $F_t = 0.33$ N for the two-layer tissue sample.

tests. One of the cylindrical samples used for the tests is depicted in Figure 4b. The sample is made from the same tissue batches as used for insertion experiments. The tissue sample is clamped in between a rigid surface on the right hand side of Figure 4a and an indenter with a circular area on the left hand side. The indenter is connected to a force sensor to measure the forces applied to the tissue sample. In order to apply pressure, the indenter is displaced to the right hand side with a constant rate of 1 mm/s for a maximum distance of 20 mm or until a force of 5 N is measured by the force sensor. Six trials of this experiment are carried out. A sample result of the compression test for the single-layer tissue sample is shown as a stress/strain curve in Figure 4c. Also shown in Figure 4c is the linear fit to the measured data, which indicates that Hooke's law $\sigma = K\varepsilon$ applies where σ is the stress occurring within the tissue sample caused by the applied strain ε. Finally, the measured tissue Young's modulus K for the single-layer tissue is 16.24 kPa. This value is close to the Young's modulus of prostate tissue [45]. The measured K for the first layer of the two-layer tissue is 21.59 kPa (K_1) and for the second layer it is 13.36 kPa (K_2).

In order to estimate the force F_t occurring at the needle tip for the phantom tissue samples, the measured needle tip deflection obtained from scenario 1 and 5 (see Table 1) for the single-layer and two-layer tissue samples, respectively, is used. It should be noted that needle tip deflection measurements obtained only from scenario 1 and 5 are used to identify the needle tip force F_t for the single- and two-layer tissue. Tip deflection measurements taken during insertions of the other scenarios are only used as ground truth for model validation. The proposed model for estimating the needle deflection shape during insertion does not take as input measured needle tip deflection. In Figure 5, the mean tip force estimate obtained from (18) for six insertion trials is plotted against the insertion depth. To determine the final constant F_t, the average of the estimated mean tip force curve is taken. Only data after 30 mm is considered (see Figure 5) for obtaining the constant tip force F_t since the data before 30 mm insertion depth is rather noisy (not reflected in plot). This is due to the fact that the needle tip deflection measured by the image-based needle tip tracking algorithm (see Section 3) contains more noise at shallow insertion depths. The resulting average tip force is $F_t = 0.29$ N for the single-layer tissue (see Figure 5a). To identify the tip force for the two-layer tissue, the two-layer model version is applied. The tip force for each layer is calculated separately but as the difference between the two is negligible, the same tip force of $F_t = 0.33$ N for the two-layer tissue is used (see Figure 5b). As can be observed, the estimates of F_t are roughly constant, which is physically understandable because the amount of tissue displacement done by the beveled tip is constant.

4.1.2. Validation Results

The measured and estimated needle tip trajectory curves are plotted in Figure 6a to Figure 6f against the insertion depth. The plots show one out of the six insertions for each scenario. Plotted also below the tip deflection is the error between measured and estimated tip deflection, the tip force F_t, and the applied lateral force F_l. The plot showing the progression of the 'Applied' force F_l is the lateral force provided to the needle-tissue model. As expected, scenario 1 and 5 depicted in Figure 6a and Figure 6e, respectively, show a very accurate estimate. The error remains within 0.8 mm for scenario 1 and 0.5 mm for scenario 5. During scenario 2, which is plotted in Figure 6b, the error monotonously increases to roughly 2 mm at the final insertion depth. The result of scenario 3 is shown in Figure 6c. Compared to scenario 2, a needle rotation is added to the otherwise equal conditions. The estimate is more accurate than the one in scenario 2 throughout insertion. After 100 mm depth, the model begins to slightly under-estimate the needle tip trajectory with a maximum error of approximately -1.5 mm at the final depth of 140 mm. A tip trajectory measurement and estimate for scenario 4 is shown in Figure 6d. Here, the error remains below 1 mm up to an insertion depth of 60 mm but slightly increases as the model under-estimates the tip trajectory beyond 60 mm depth with a maximum error of approximately 1.5 mm at the fi-

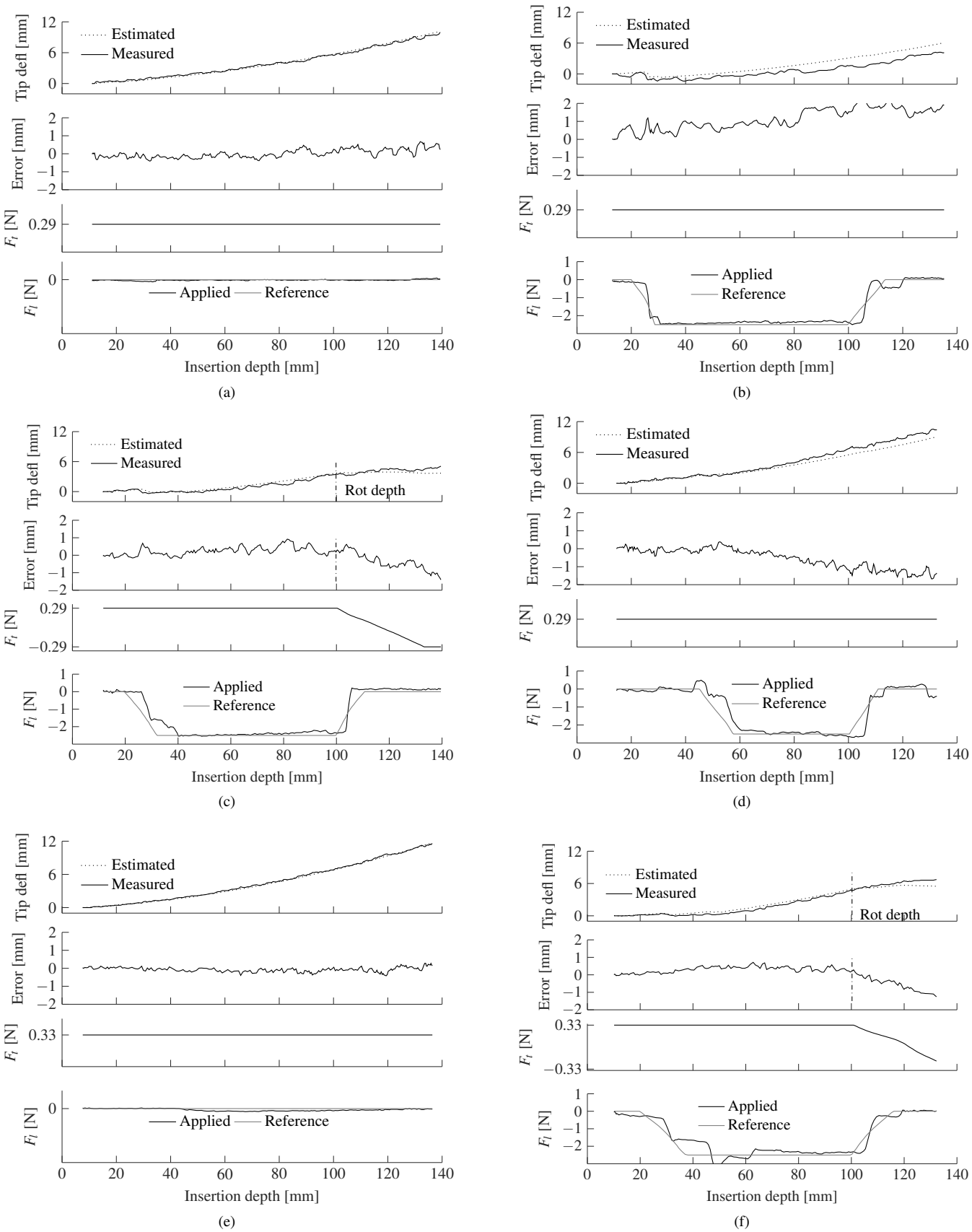

Figure 6: Results for needle tip trajectory estimation for experimental scenarios (a) without any corrective measures, (b) $F_l = -2.5$ N and $d_l = 20$ mm, (c) $F_l = -2.5$ N, $d_l = 20$ mm, and $d_r = 100$ mm, (d) $F_l = -2.5$ N and $d_l = 45$ mm, (e) without any corrective measures and two-layer tissue, and $F_l = -2.5$ N, $d_l = 20$ mm, $d_r = 100$ mm and two-layer tissue.

Table 2: Statistical results of the experimental scenarios. Results of a two-sample t-test are shown (h). The mean error between measured and estimated needle tip trajectory ($\bar{e}$) and the standard error ($\sigma/\sqrt{n}$) over six trials for four insertion depths are listed. Measured and estimated tip trajectories over 6 trials are compared.

Trial #	Insertion depth [mm]									
	30		60		90		120		140	
	h	$\lvert\bar{e}\rvert \pm \frac{\sigma}{\sqrt{n}}$	h	$\lvert\bar{e}\rvert \pm \frac{\sigma}{\sqrt{n}}$	h	$\lvert\bar{e}\rvert \pm \frac{\sigma}{\sqrt{n}}$	h	$\lvert\bar{e}\rvert \pm \frac{\sigma}{\sqrt{n}}$	h	$\lvert\bar{e}\rvert \pm \frac{\sigma}{\sqrt{n}}$
1	$\bar{r}$	0.19±0.1	$\bar{r}$	0.33±0.21	$\bar{r}$	0.51±0.27	$\bar{r}$	0.7±0.37	$\bar{r}$	0.83±0.44
2	r	0.87±0.22	r	1±0.21	r	0.92±0.25	r	1.26±0.39	r	1.29±0.39
3	$\bar{r}$	0.25±0.15	$\bar{r}$	0.55±0.24	$\bar{r}$	0.65±0.3	$\bar{r}$	0.86±0.38	$\bar{r}$	1.22±0.5
4	$\bar{r}$	0.38±0.2	$\bar{r}$	0.41±0.18	r	0.89±0.1	r	1.24±0.12	r	1.48±0.18
5	$\bar{r}$	0.11±0.05	$\bar{r}$	0.11±0.05	$\bar{r}$	0.35±0.14	$\bar{r}$	0.29±0.22	$\bar{r}$	0.46±0.21
6	$\bar{r}$	0.15±0.09	$\bar{r}$	0.36±0.19	$\bar{r}$	0.43±0.23	$\bar{r}$	1.11±0.37	r	1.98±0.41

r denotes that the null hypothesis must be rejected and $\bar{r}$ denotes that it can not be rejected at the 5% significance level.

nal insertion depth. Scenario 6, where two-layer tissue is used, shows an accurate estimate with an error of less than 1 mm below 100 mm insertion depth. The estimation performance is very similar to scenario 2 where the same lateral force profile and axial needle rotation depth are applied, while during scenario 6, the needle is inserted into two-layer tissue. Beyond a depth of 100 mm, the error monotonously increases to roughly 2 mm at the final insertion depth.

To further examine the accuracy of the needle-tissue model, a statistical analysis is provided. In order to show whether the estimation error is statistically significant, a two-sample t-test is carried out. The null hypothesis of the test states that no significant difference exists between the measured and estimated needle tip trajectory. The test has a 5% significance level and the sample size is six. The results listed in Table 2 indicate whether the null hypothesis must be rejected or not. Furthermore, in Table 2, the mean absolute error $|\bar{e}|$ between the measured and estimated needle tip trajectory and the standard error $\sigma/\sqrt{n}$ across the $n = 6$ runs are listed. The results presented in Table 2 confirm the observations made in Figure 6 and described further above.

5. Deflection Control Simulation

A needle tip deflection control simulation study is carried out with the purpose of assessing the performance and limitations of a simple ad-hoc controller that combines the two control inputs lateral force and axial needle rotation. Moreover, advantages of combining the two control inputs are explored. The needle tip deflection is controlled through a combination

Table 3: The control input combinations.

Control scenario	Lateral force application	Axial rotation
1	no	no
2	no	yes
3	yes	no
4	yes	yes

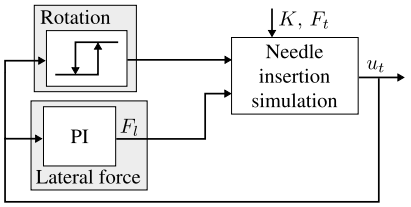

Figure 7: The schematic for simulated control of needle tip deflection (u_t) using multiple 180° axial needle rotations and application of lateral force F_l. The 180° axial needle rotation is commanded by a bang-bang controller. The needle rotations from 0° to 180° and vice versa are triggered when a tip deflection threshold is exceeded.

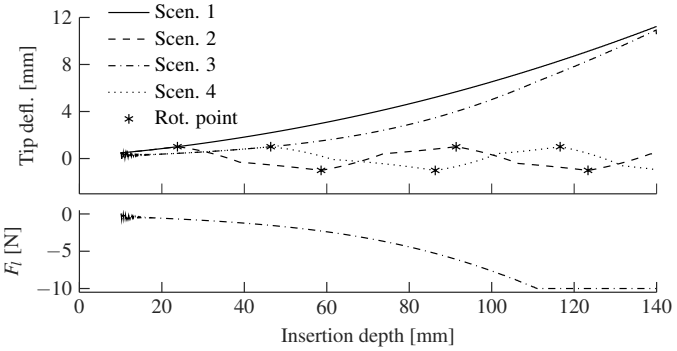

Figure 8: The needle tip deflection trajectories during needle insertion (top sub-plot) and the lateral force F_l applied during control scenario 3 (bottom sub-plot).

of 180° axial needle rotation and lateral force F_l application. The control method is schematically illustrated in Figure 7. The controller for needle rotation is based on a bang-bang controller where a needle rotation by 180° is triggered when a tip deflection magnitude of $\tau = 1$ mm is exceeded. The applied lateral force F_l is adjusted by a PI controller where the reference tip deflection is zero. The previously identified model parameter values $K = 16.24$ kPa and $F_t = 0.29$ N for the single-layer phantom tissue sample are used for the simulation. The four considered control scenarios are listed in Table 3. In control scenario 1, the needle tip deflection is deliberately not controlled for performance assessment of control scenario 2 to 4. The PI gains of the lateral force controller are empirically determined to result in the best possible performance. Figure 8 shows the simulation results for the four control scenarios where the top sub-plot shows the needle tip deflection trajectories and the bottom sub-plot shows the applied lateral force F_l during control scenario 3. While only using lateral force to control needle tip deflection (control scenario 3), the controller is initially able to minimize the tip deflection but fails with increasing insertion depth. It can be observed that the needle tip deflection can not be reduced at greater insertion depths despite the increasing magnitude of F_l until the saturation point of 10 N is reached. The reason for the decreased ability of the lateral force actuation to move the needle tip laterally is due to the needle being supported by tissue and the needle's decrease in resistance to bending with increasing length. The limitations of the lateral force with respect to needle insertion depth is further studied in Section 6. When controlled axial needle rotation is added to lateral force control

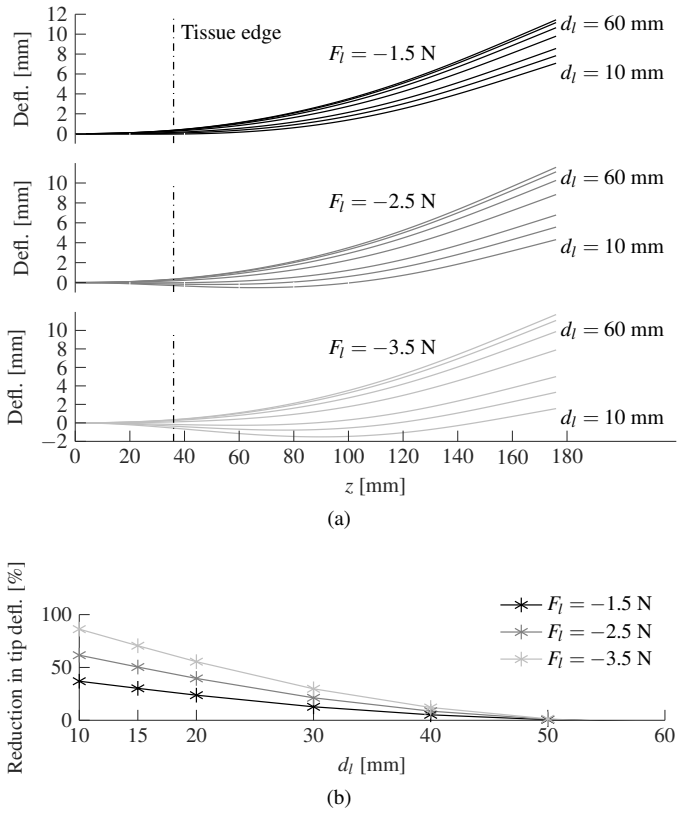

Figure 9: The effect of lateral force applied at various d_l. (a) Simulation results for needle curvature with three different lateral forces F_l applied at seven different depths $d_l = [10\ 15\ 20\ 30\ 40\ 50\ 60]$ mm. (b) The influence of d_l on needle tip deflection after needle insertion is stopped. The plot shows the amount of reduction of needle deflection in percent at the final insertion depth for various d_l and F_l. The comparison is made with respect to needle deflection with $F_l = 0$ and no axial rotation.

during insertion (control scenario 4), the needle tip deflection can be reduced to below 1 mm at the final insertion depth with three rotations. When only axial rotation is considered without lateral force as in control scenario 2, the needle tip deflection also remains within 1 mm during insertion. However, four axial needle rotations are necessary to achieve the same outcome compared to control scenario 4.

6. Sensitivity Analysis

This section provides results of a sensitivity analysis with respect to the lateral force F_l and its depth of application d_l in order to highlight achievable steering goals with a focus on minimizing the needle's deflection and the influence of d_l on needle deflection.

Needle insertion simulations using the proposed model are carried out with the same parameters $F_t = 0.29$ N and $K = 16.24$ kPa as obtained for the phantom tissue used for experimental validation. Three different constant lateral force magnitudes, F_l = [-1.5 -2.5 -3.5] N, and seven depths at which application of F_l is started, $d_l = [10\ 15\ 20\ 30\ 40\ 50\ 60]$ mm, are considered, resulting in 21 simulations.

The simulation results are plotted in Figure 9 where Figure 9a shows simulated needle curvatures at the final insertion depth of 140 mm. Each plot shows needle deflection shapes for one of three investigated lateral forces and all considered depths of force application. By increasing the lateral force magnitude applied to the needle shaft, a smaller needle deflection can be achieved compared to a lower magnitude. Moreover, shallower depths of force application, e.g., $d_l \leq 20$ mm, result in the least needle deflection, which is expected. The reasons for this are further discussed in Section 7. Figure 9b provides a supplementary analysis of the plots provided in Figure 9a with an emphasis on the needle tip deflection at the final insertion depth of 140 mm and how it is influenced by the depth of application of the lateral force. It shows the amount by which needle tip deflection can be reduced (in percent) for increasing lateral force magnitudes and their associated depths of application. The comparison is made with respect to needle deflection without steering inputs. An application depth of 10 mm and a lateral force magnitude of -3.5 N shows at 90% (the highest) reduction, while a magnitude of -1.5 N shows approximately 40% (the lowest) reduction. The curves furthermore suggest a decline in the reduction in tip deflection at increasing force application depths with almost no reduction remaining at a force application depth of 60 mm.

7. Discussion

The results of the experimental validation show that the differences between the measured and estimated trajectories are not statistically significant for most cases up to 120 mm insertion depth according to Table 2. This suggests that the lateral needle displacement caused by the application of the lateral force F_l is modeled well. According to the t-test results, the estimated and measured tip trajectories are significantly different during scenario 2 and scenario 4 where the error does not exceed 1.5 mm at the final insertion depth. This demonstrates that the proposed model represents the physical needle-tissue system well considering that the tissue stiffness K used as input to the model represents a physical property of the phantom tissue sample. When considering scenarios 5 and 6, the multi-layer version of the deflection model shows a similar performance than the single-layer version.

The error significance, however, increases during most scenarios as the needle approaches the final insertion depth. According to Table 2, the error significance increases with an overall maximum $|\bar{e}|$ of 1.98 mm occurring during scenario 6 and insertion depth 140 mm. Considering that a standard brachytherapy needle's inner diameter and thus the radioactive seed diameter is about 1 mm, and that the error compared to the tip deflection without correction is approximately 80% less, this error is an acceptable deviation. Moreover, when the deflection model is applied to needle steering, where a model-based controller would adjust the needle deflection using lateral actuation and axial rotation to reach a defined target, the controller can also adjust the model parameters in order to account for and correct model prediction errors using online feedback of the needle deflection (e.g., ultrasound-based).

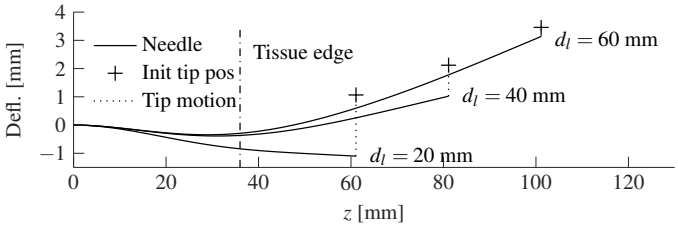

Figure 10: Needle curvatures for three different simulations with various depths of application d_l. The change in needle tip position is shown during the switch from $F_l = 0$ N to the full magnitude of $F_l = -3.5$ N.

In Section 5, a rudimentary ad-hoc control simulation is presented for the minimization of needle tip deflection during insertion. The control parameters are empirically determined to yield best possible results for the specific combination of model parameters K and F_t. Due to the limitations of lateral force application on needle tip deflection shown in Section 6, the lateral force controller is not able by itself to minimize needle tip deflection at greater insertion depths. Therefore, using a controller that is based purely on the feedback of the current needle tip deflection is not enough for reliable and adaptive needle deflection control. To achieve deflection minimization results shown in Section 6 by applying lateral force only, a more sophisticated controller is needed that uses the proposed model for prediction-based control decisions and takes into account the knowledge gained from Section 6.

When a combination of lateral force and axial rotation is applied for needle tip deflection control, less needle rotations are necessary to achieve a similar needle tip trajectory than when only axial needle rotation is used. Due to the nonlinear nature of the needle-tissue system that has no equilibrium point other than when the insertion speed is zero, as long as the needle moves, its trajectory will diverge from a straight line, which is physically understandable due to the effect of the beveled tip. Therefore, if the goal is to keep the needle tip on straight line (as it is in prostate brachytherapy due to assumptions made during seed deposition planning), the axial rotation input needs to be invoked continually to keep the tip deflection below a threshold. However, with two control inputs, namely the axial rotation and the lateral force, the level of activity or magnitude of each control input is less. Thus, since excessive use of axial rotation results in tissue drilling effects [39], the availability of an additional control input (the lateral force) is highly beneficial.

The results of the sensitivity analysis with respect to reduction of needle deflection presented in Section 6 are a somewhat expected outcome based on the observations made in Section 5. The behavior of the needle when the lateral force is applied at varying depths is further illustrated in Figure 10. There is more tissue support as the needle is inserted deeper into tissue, and the needle's bending stiffness with increasing length is reduced. As a result of this, a needle that is inserted deeper into tissue bends more rather than the entire needle shaft being moved laterally. Therefore, the needle tip is also subject to less lateral motion when F_l is applied at greater depths, which in turn significantly diminishes the potential to reduce needle deflection as shown in Figure 9b.

The results presented in Section 6 show that a combination of lateral force F_l and depth of application d_l exists that results in a 100% reduction of needle tip deflection ($F_l = -3.5$ N and $d_l = 10$ mm, see Figure 9b). Therefore, it is possible to fully eliminate needle deflection by only applying lateral force. Combining lateral force with rotation, however, provides an additional method of steering, meaning that less lateral force is necessary to obtain the same outcome for reduction of needle tip deflection.

The possible applications for the model presented in this work are on-line needle deflection estimation and prediction. A control algorithm using a model-based predictive control (MPC) approach can be designed for automated needle steering using an appropriate combination of lateral force F_l and needle rotation based on the knowledge gained from Section 5 and Section 6. The control algorithm will also be able to correct for the model errors apparent from Section 4 by adjusting model parameters or control inputs accordingly.

8. Conclusion & Future Work

This work proposes a novel method for automated needle steering during insertion into soft tissue, and a model that is used to estimate the needle deflection during insertion based on the novel steering method. The method combines the application of a lateral force near the needle entry point into tissue with the axial needle rotation. An energy-based model is introduced for the estimation and prediction of needle deflection during insertion taking into account the lateral force and the axial rotation. The model is appropriate for model-based needle deflection control. It is experimentally validated and shown to estimate needle tip deflection with good accuracy for single and two-layer tissue. Simulations of needle insertions using the proposed model study the steering effects, potentials and limitations of lateral force application in terms of reducing needle tip deflection. The simulation results confirm the assumption that the influence of lateral force on needle curvature inside tissue is reduced with increasing insertion depth, but also demonstrate that it is possible to reduce needle deflection by a high margin of 90%.

This paper represents a first step towards designing control methods for needle deflection using a combination of lateral force and axial rotation. Thus, in our future work, the model will be used to design controllers to automatically steer the needle towards a desired target while the control algorithm takes informed decisions on appropriate control actions during insertion.

Acknowledgment

This work was supported by the Canada Foundation for Innovation (CFI) under grant LOF 28241, the Alberta Innovation and Advanced Education Ministry under Small Equipment Grant RCP-12-021, the Natural Sciences and Engineering Research Council (NSERC) of Canada under grant CHRP

446520, the Canadian Institutes of Health Research (CIHR) under grant CPG 127768, the Alberta Innovates - Health Solutions (AIHS) under grant CRIO 201201232 and by a University of Alberta startup grant. The authors would like to thank Abdoreza Farhangi for assistance on the mechanical design of the robotic assistant system prototype, and Qingxin Yuan and Shayan Meschian for assistance with needle insertion experiments.

References

[1] C. Simone, A. Okamura, Modeling of needle insertion forces for robot-assisted percutaneous therapy, in: Proceedings of the 2002 IEEE International Conference on Robotics and Automation, Vol. 2, 2002, pp. 2085–2091.

[2] A. Okamura, C. Simone, M. O'Leary, Force modeling for needle insertion into soft tissue, IEEE Transactions on Biomedical Engineering 51 (10) (2004) 1707–1716.

[3] S. DiMaio, S. Salcudean, Needle Steering and Motion Planning in Soft Tissues, IEEE Transactions on Biomedical Engineering 52 (6) (2005) 965–974.

[4] S. Misra, K. B. Reed, A. S. Douglas, K. T. Ramesh, A. M. Okamura, Needle-tissue interaction forces for bevel-tip steerable needles, in: Proceedings of the 2nd Biennial IEEE/RAS-EMBS International Conference on Biomedical Robotics and Biomechatronics, BioRob, 2008, pp. 224–231.

[5] S. Misra, K. B. Reed, B. W. Schafer, K. T. Ramesh, A. M. Okamura, Observations and models for needle-tissue interactions, in: Proceedings of the 2009 IEEE International Conference on Robotics and Automation, 2009, pp. 2687–2692.

[6] H. Kataoka, T. Washio, M. Audette, K. Mizuhara, A Model for Relations Between Needle Deflection, Force, and Thickness on Needle Penetration, in: Medical Image Computing and Computer-Assisted Intervention - MICCAI 2001, Vol. 2208 of Lecture Notes in Computer Science, Springer, Berlin, Heidelberg, 2001, Ch. 115, pp. 966–974.

[7] N. Abolhassani, R. V. Patel, Deflection of a Flexible Needle during Insertion into Soft Tissue, in: IEEE EMBS Annual International Conference, IEEE, 2006, pp. 3858–3861.

[8] N. Abolhassani, R. Patel, F. Ayazi, Minimization of needle deflection in robot-assisted percutaneous therapy, The International Journal of Medical Robotics and Computer Assisted Surgery 3 (2) (2007) 140–148.

[9] S. Misra, K. B. Reed, B. W. Schafer, K. T. Ramesh, A. M. Okamura, Mechanics of flexible needles robotically steered through soft tissue, The International Journal of Robotics Research 29 (13) (2010) 1640–1660.

[10] R. Roesthuis, Y. V. Veen, A. Jahya, S. Misra, Mechanics of needle-tissue interaction, in: 2011 IEEE/RSJ International Conference on Intelligent Robots and Systems (IROS), IEEE, 2011, pp. 2557–2563.

[11] R. J. Roesthuis, M. Abayazid, S. Misra, Mechanics-based model for predicting in-plane needle deflection with multiple bends, in: Proceedings of the 2012 IEEE RAS and EMBS International Conference on Biomedical Robotics and Biomechatronics, 2012, pp. 69–74.

[12] M. Khadem, B. Fallahi, C. Rossa, R. S. Sloboda, N. Usmani, M. Tavakoli, A mechanics-based model for simulation and control of flexible needle insertion in soft tissue, in: Proceedings of the 2015 IEEE International Conference on Robotics and Automation (ICRA), IEEE, 2015, pp. 2264–2269.

[13] T. Lehmann, C. Rossa, N. Usmani, R. Sloboda, M. Tavakoli, A virtual sensor for needle deflection estimation during soft-tissue needle insertion, in: 2015 IEEE International Conference on Robotics and Automation (ICRA), IEEE, 2015, pp. 1217–1222.

[14] M. Khadem, C. Rossa, N. Usmani, R. S. Sloboda, M. Tavakoli, A Two-body Rigid/Flexible Model of Needle Steering Dynamics in Soft Tissue, IEEE/ASME Transactions on Mechatronics 21 (5) (2016) 2352–2364.

[15] T. Lehmann, C. Rossa, N. Usmani, R. S. Sloboda, M. Tavakoli, A Real-Time Estimator for Needle Deflection During Insertion Into Soft Tissue Based on Adaptive Modeling of Needle-Tissue Interactions, IEEE/ASME Transactions on Mechatronics 21 (6) (2016) 2601–2612.

[16] C. Rossa, M. Khadem, R. Sloboda, N. Usmani, M. Tavakoli, Adaptive Quasi-Static Modelling of Needle Deflection During Steering in Soft Tissue, IEEE Robotics and Automation Letters 1 (2) (2016) 916–923.

[17] H. Lee, J. Kim, Estimation of Needle Deflection in Layered Soft Tissue for Robotic Needle Steering, in: E. Menegatti, N. Michael, K. Berns, H. Yamaguchi (Eds.), Intelligent Autonomous Systems 13: Proceedings of the 13th International Conference IAS-13, Springer International Publishing, Cham, 2016, pp. 1133–1144.

[18] R. J. Webster, J. S. Kim, N. J. Cowan, G. S. Chirikjian, A. M. Okamura, Nonholonomic modeling of needle steering, Int. J. Rob. Res. 25 (5-6) (2006) 509–525.

[19] D. Glozman, M. Shoham, Image-guided robotic flexible needle steering, IEEE Transactions on Robotics 23 (3) (2007) 459–467.

[20] M. Abayazid, R. Roesthuis, R. Reilink, S. Misra, Integrating Deflection Models and Image Feedback for Real-Time Flexible Needle Steering, IEEE Transactions on Robotics 29 (2) (2013) 542–553.

[21] S. Patil, J. Burgner, R. J. Webster, R. Alterovitz, Needle steering in 3-D Via rapid replanning, IEEE Transactions on Robotics 30 (4) (2014) 853–864.

[22] B. Fallahi, M. Khadem, C. Rossa, R. Sloboda, N. Usmani, M. Tavakoli, Extended Bicycle Model for Needle Steering in Soft Tissue, in: Proceedings of the 2015 IEEE/RSJ International Conference on Intelligent Robots and Systems (IROS), 2015, pp. 4375–4380.

[23] S. DiMaio, S. Salcudean, Needle insertion modelling and simulation, in: IEEE International Conference on Robotics and Automation (ICRA), Vol. 2, 2002, pp. 2098–2105.

[24] T. Lehmann, C. Rossa, R. Sloboda, N. Usmani, M. Tavakoli, Needle path control during insertion in soft tissue using a force-sensor-based deflection estimator, in: Proceedings of the 2016 IEEE International Conference on Advanced Intelligent Mechatronics (AIM), IEEE, 2016, pp. 1174–1179.

[25] R. Webster, J. Memisevic, A. Okamura, Design Considerations for Robotic Needle Steering, in: Proceedings of the 2005 IEEE International Conference on Robotics and Automation, 2005. ICRA 2005, 2005, pp. 3588 – 3594.

[26] B. Fallahi, C. Rossa, R. S. Sloboda, N. Usmani, M. Tavakoli, Sliding-Based Switching Control for Image-Guided Needle Steering in Soft Tissue, IEEE Robotics and Automation Letters 1 (2) (2016) 860–867.

[27] D. Stoianovici, L. L. Whitcomb, J. H. Anderson, R. H. Taylor, L. R. Kavoussi, A modular surgical robotic system for image guided percutaneous procedures, in: W. M. Wells, A. Colchester, S. Delp (Eds.), Medical Image Computing and Computer-Assisted Interventation — MICCAI'98: First International Conference, Springer Berlin Heidelberg, Berlin, Heidelberg, 1998, pp. 404–410.

[28] K. Cleary, M. Freedman, M. Clifford, D. Lindisch, S. Onda, L. Jiang, Image-guided robotic delivery system for precise placement of therapeutic agents, Journal of Controlled Release 74 (1Ű3) (2001) 363–368.

[29] J. Hong, T. Dohi, M. Hashizume, K. Konishi, N. Hata, An ultrasound-driven needle-insertion robot for percutaneous cholecystostomy, Physics in Medicine and Biology 49 (3) (2004) 441–455.

[30] C. M. Schneider, A. M. Okamura, G. Fichtinger, A robotic system for transrectal needle insertion into the prostate with integrated ultrasound, in: Proceedings of the 2004 IEEE International Conference on Robotics and Automation, Vol. 1, 2004, pp. 365–370.

[31] M. Muntener, A. Patriciu, D. Petrisor, D. Mazilu, H. Bagga, L. Kavoussi, K. Cleary, D. Stoianovici, Magnetic resonance imaging compatible robotic system for fully automated brachytherapy seed placement, Urology 68 (6) (2006) 1313–1317.

[32] Z. Neubach, M. Shoham, Ultrasound-Guided Robot for Flexible Needle Steering, IEEE Transactions on Biomedical Engineering 57 (4) (2010) 799–805.

[33] G. Fichtinger, T. L. DeWeese, A. Patriciu, A. Tanacs, D. Mazilu, J. H. Anderson, K. Masamune, R. H. Taylor, D. Stoianovici, System for Robotically Assisted Prostate Biopsy and Therapy with Intraoperative {CT} Guidance, Academic Radiology 9 (1) (2002) 60–74.

[34] G. Fichtinger, J. P. Fiene, C. W. Kennedy, G. Kronreif, I. Iordachita, D. Y. Song, E. C. Burdette, P. Kazanzides, Robotic assistance for ultrasound-guided prostate brachytherapy, Medical Image Analysis 12 (5) (2008) 535–545.

[35] D. Y. Song, E. C. Burdette, J. Fiene, E. Armour, G. Kronreif, A. Deguet, Z. Zhang, I. Iordachita, G. Fichtinger, P. Kazanzides, Robotic needle

guide for prostate brachytherapy: Clinical testing of feasibility and performance, Brachytherapy 10 (1) (2011) 57–63.

[36] S. E. Song, J. Tokuda, K. Tuncali, C. M. Tempany, E. Zhang, N. Hata, Development and Preliminary Evaluation of a Motorized Needle Guide Template for MRI-Guided Targeted Prostate Biopsy, IEEE Transactions on Biomedical Engineering 60 (11) (2013) 3019–3027.

[37] S. E. Salcudean, T. D. Prananta, W. J. Morris, I. Spadinger, A robotic needle guide for prostate brachytherapy, in: Proceedings of the 2008 IEEE International Conference on Robotics and Automation, IEEE, 2008, pp. 2975–2981.

[38] C. Rossa, M. Tavakoli, Issues in closed-loop needle steering, Control Engineering Practice 62 (2017) 55–69.

[39] M. A. Meltsner, N. J. Ferrier, B. R. Thomadsen, Observations on rotating needle insertions using a brachytherapy robot, Physics in Medicine and Biology 52 (19) (2007) 6027–6037.

[40] N. J. Cowan, K. Goldberg, G. S. Chirikjian, G. Fichtinger, R. Alterovitz, K. B. Reed, V. Kallem, W. Park, S. Misra, A. M. Okamura, Robotic needle steering: Design, modeling, planning, and image guidance, in: Surgical Robotics: Systems Applications and Visions, Springer US, Boston, MA, 2011, pp. 557–582.

[41] J. Reddy, An Introduction to the Finite Element Method, 2nd Edition, McGraw-Hill series in mechanical engineering, McGraw-Hill, 1993.

[42] G. Genta, Vibration Dynamics and Control, Mechanical Engineering Series, Springer, New York, NY, USA, 2008.

[43] C. Rossa, N. Usmani, R. Sloboda, M. Tavakoli, A Hand-Held Assistant for Semiautomated Percutaneous Needle Steering, IEEE Transactions on Biomedical Engineering 64 (3) (2017) 637–648.

[44] J. Carriere, C. Rossa, R. Sloboda, N. Usmani, M. Tavakoli, Real-time needle shape prediction in soft-tissue based on image segmentation and particle filtering, in: 2016 IEEE International Conference on Advanced Intelligent Mechatronics (AIM), IEEE, 2016, pp. 1204–1209.

[45] K. Hoyt, B. Castaneda, M. Zhang, P. Nigwekar, P. A. di Sant'agnese, J. V. Joseph, J. Strang, D. J. Rubens, K. J. Parker, Tissue elasticity properties as biomarkers for prostate cancer., Cancer biomarkers : section A of Disease markers 4 (4-5) (2008) 213–25.